Journal of Oceanography, Vol. 64, pp. 777 to 788, 2008

The Kuroshio near the Luzon Strait and Circulation in the Northern South China Sea during August and September 1994

YAOCHU YUAN*, GUANGHONG LIAO and CHENGHAO YANG

State Key Laboratory of Satellite Ocean Environment Dynamics, Second Institute of Oceanography, State Oceanic Administration, Hangzhou 310012, P.R. China

(Received 7 November 2007; in revised form 14 March 2008; accepted 21 March 2008)

Wind data from NCEP and hydrographic data obtained from August 28 to September 10, 1994 have been used to compute circulation in the northern South China Sea and near Luzon Strait using three-dimensional diagnostic models with a modified inverse method. The numerical results are as follows: the main Kuroshio is located above 400 m levels near Taiwan's eastern coast and above 800 m levels away from it. Near Luzon Strait above 400 m levels a branch of the Kuroshio joins with a part of the northward current, which comes from an area west of Luzon's western coast and intrudes northwestward, then it branchs into western and eastern parts near 20°30′ N. The eastern part flows northward into an area east of Taiwan, while its western part continues to intrude northwestward, flowing through an area southwest of Taiwan. Net westward intruded volume transport through longitude Section AB at 121°00′ E from 19°00′ N to 21°43′ N is about 3.5×10^6 m^3s^{-1} in a layer above 400 m levels. The anticyclonic eddies W1 and W3 exist above 700 m levels east of Dongsha Islands and below 200 m levels in the eastern part of the region, respectively. The circulation in the middle region is dominated mainly by a basin-scale cyclonic gyre, and consists of three cyclonic eddies. Strong upwelling occurs in the middle region. The joint effect of baroclinity and relief and interaction between wind stress and relief both are important for real forcing of flow across contours of fH^{-1} in effecting the circulation pattern.

Keywords:
- Intrusion of a branch of Kuroshio into the SCS,
- three-dimensional diagnostic modeling,
- modified inverse method,
- cyclonic and anti-cyclonic eddies,
- basin-scale cyclonic gyre,
- real forcing of flow across contours of fH^{-1}.

1. Introduction

The Luzon Strait is the deepest passage linking the South China Sea (SCS) with the Pacific Ocean. Some studies have looked at the westward intrusion of the Kuroshio into the SCS via the Luzon Strait. The volume transport (VT) through the Luzon Strait, called the Luzon Strait Transport (LST) hereafter, is essentially westward (Qu, 2002; Qu *et al*., 2004). Using available historical temperature profiles combined with climatological temperature-salinity relationships in the SCS, Qu (2000) pointed out that the LST (relative to 400 db) was estimated to be of order 3.0×10^6 m^3s^{-1} in the mean, and had a seasonal cycle dominating the annual signal, with a maximum (5.3×10^6 m^3s^{-1}) in Jan.–Feb. and a minimum (0.2×10^6 m^3s^{-1}) in June–July. Various numerical models have been used to obtain the different values of annual mean LST, viz., 2.4×10^6 m^3s^{-1} (Qu *et al*., 2004), 6.5×10^6 m^3s^{-1} (Chu and Li, 2000), 6.4×10^6 m^3s^{-1} (Fang *et al*., 2002), 2.0×10^6 m^3s^{-1} (Xue *et al*., 2004), 4.1×10^6 m^3s^{-1} in the mean (Cai *et al*., 2005) and so on. In addition to the abovementioned numerical studies, based on the CTD data obtained in March of 1992 and Aug.–Sep. of 1994 cruises, Xu *et al*. (1995) and Xu and Su (1997) both discussed the hydrographic analysis of the intrusion of Kuroshio water into the SCS.

The main objectives of this paper are as follows: 1) to describe the variation of the main Kuroshio in horizontal and vertical directions; 2) to study an intruded northwestward branch of the Kuroshio into the SCS through the Luzon Strait above 400 m levels, and the current structure and the estimation of its net westward intruded volume transport through the Luzon Strait in this cruise; 3) to discuss and describe the circulation in the northern South China Sea, especially the variation of the anti-cyclonic and cyclonic eddies in horizontal and vertical directions in this cruise. The joint effect of the

* Corresponding author. E-mail: yuanyc2@sio.zj.edu.cn

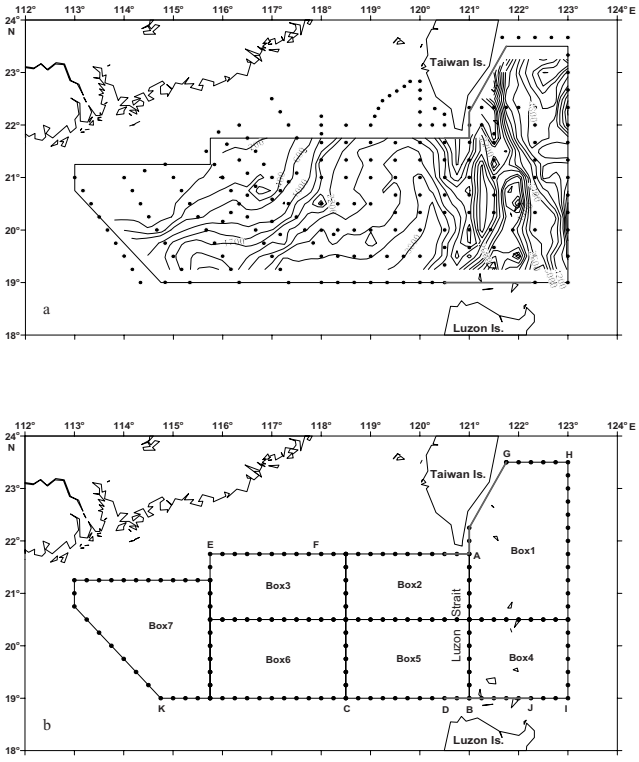

Fig. 1. (a) Location of observed hydrographic stations and bottom topography; (b) computation boxes in the computation region during August 28 to September 10, 1994 (heavy lines denote the solid boundary and thin lines denote the open boundary).

baroclinity and relief (JEBAR) and the interaction between the wind stress and relief (IBWSR) terms are discussed, since they are both important for the real forcing of flow across contours of fH^{-1} in effecting the pattern of circulation. In Section 2, a three-dimensional diagnostic model of ocean circulation (Yuan *et al*., 1986, 2007; Yuan and Su, 1988) as well as a modified inverse method (MIM) (Yuan *et al*., 1992) are used to study the circulation in the region investigated, on the basis of the hydrographic data obtained (see Fig. 1) southeast of Taiwan and near the Luzon Strait and in the northern South China Sea (SCS) during August 28 to September 10, 1994. Section 3 discusses the wind field obtained from NCEP data and the hydrographic analyses. Section 4 discusses diagnostic current results from field data input to a three-dimensional model with the modified inverse method. This is the main content of the paper. Section 5 presents ours conclusions.

2. Diagnostic Model with the Modified Inverse Method

On the basis of the hydrographic and wind data obtained in the investigated regions southeast of Taiwan and near the Luzon Strait and in the northern South China Sea (SCS) during August 28 to September 10, 1994 during the cooperative cruises of the R/V Xiangyanghong No. 14, R/V Yanping No. 1, R/V Haiyan No. 1 and R/V Haiyan No. 3, a three-dimensional diagnostic model of ocean circulation with the modified inverse method is used to study the circulation in the investigated area.

The modified inverse method (MIM) described by Yuan *et al*. (1992, 2005) and Liu *et al*. (2000) is used to compute the current structure and volume transport and the stream function in the computational region (Fig. 1(b)). In this method, the following three assumptions are made:

(1) The ocean current is in the steady state, and the vertical friction term in the momentum equation is retained.

(2) All convection terms and the vertical diffusion term in the density and salt equations are retained, but the horizontal diffusion terms are negligible.

(3) The β-effect is also considered.

For a three-dimensional diagnostic model of ocean circulation, we assume that: 1) the density field ρ is given; 2) the wind field over the area is obtained from wind data; 3) the β effect is considered. As in a previous study (Yuan and Su, 1988), both the non-linear and lateral friction terms in the momentum equation are negligible for the circulation in the South China Sea, as revealed by a dimensional analysis of the momentum equation. We assume a constant vertical eddy coefficient A_z and use a right-hand Cartesian coordinate system with the z axis directed upward, so the steady state momentum and continuity equations refer to Yuan *et al*. (1986, 2007), in which the Boussinesq assumption has been made.

The boundary conditions at the surface are:

$$\rho_0 A_z \left(\frac{\partial u}{\partial z}\right)_\varsigma = \tau_s^x, \tag{1}$$

$$\rho_0 A_z \left(\frac{\partial \upsilon}{\partial z}\right)_\varsigma = \tau_s^y, \tag{2}$$

$$w_\varsigma = 0, \tag{3}$$

where ρ_0 is a constant density, ρ and p are anomalies of density and pressure, respectively, u and v are the eastward and northward component of the velocity, and the other notations are standard. $\vec{\tau}_s = (\tau_s^x, \tau_s^y)$ is the wind stress vector and ς is the sea surface elevation.

The no-slip boundary conditions at the bottom H are

$$u = v = w = 0. \tag{4}$$

The slip boundary conditions at the bottom H are

$$\rho_0 A_z \left(\frac{\partial u}{\partial z}\right)_b = \tau_b^x, \tag{5}$$

$$\rho_0 A_z \left(\frac{\partial \upsilon}{\partial z}\right)_b = \tau_b^y, \tag{6}$$

$$w_{-H} = -\left(u_H \frac{\partial H}{\partial x} + \upsilon_H \frac{\partial H}{\partial y}\right), \tag{7}$$

where $\vec{\tau}_b(\tau_b^x, \tau_b^y)$ is the bottom friction stress vector.

Vertical integration of the static pressure equation leads to

$$p = \rho_0 g\varsigma + \int_z^0 \rho g dz. \tag{8}$$

The governing equation for the stream function ψ is obtained from the vorticity equation of the vertically integrated form of momentum equation as follows (see Yuan *et al*., 2007):

$$\begin{aligned}&\frac{\partial}{\partial x}\left(\frac{B}{H^2}\frac{\partial \psi}{\partial x}\right)+\frac{\partial}{\partial y}\left(\frac{B}{H^2}\frac{\partial \psi}{\partial y}\right)+\frac{f}{H^2}J(H,\psi)+\frac{\beta}{H}\left(\frac{\partial \psi}{\partial x}\right)\\ &=\frac{g}{\rho_0 H^2}J\left(H,\int_{-H}^0 z\rho dz\right)+\frac{1}{\rho_0 H}\left(\frac{\partial \tau_s^y}{\partial x}-\frac{\partial \tau_s^x}{\partial y}\right)\\ &\quad+\frac{1}{\rho_0 H^2}\left[\frac{\partial H}{\partial y}\tau_s^x-\frac{\partial H}{\partial x}\tau_s^y\right],\end{aligned} \tag{9}$$

where:

$$\vec{V} = \frac{1}{H}\vec{k}\times\nabla\psi = \left(\frac{1}{H}\int_{-H}^0 u dz, \frac{1}{H}\int_{-H}^0 \upsilon dz\right). \tag{10}$$

Here $\vec{V}$ denotes the vertical average of the horizontal velocity vector, B is the bottom friction coefficient and J is the Jacobian operator. On the right-hand side of Eq. (9) the first term is due to the joint effect of the baroclinity and relief (JEBAR), the second term is due to the effect of wind stress rotation (WSR), while the third term is due to the interaction between the wind stress and relief (IBWSR). Mertz and Wright (1992) discussed in detail the physical interpretation of the JEBAR term, emphasizing that JEBAR may be regarded as a real forcing term when the density field is specified, as in a diagnostic calculation of the circulation. Here we also discuss the physical interpretation of the JEBAR term in a diagnostic calculation of the circulation. We rewrite Eq. (9) in the form

$$\begin{aligned}&J\left(\psi,\frac{f}{H}\right)\\ &=curl_z\left[\frac{\vec{\tau}_s-\rho_0\nabla\Omega}{\rho_0 H}\right]-\left[\frac{\partial}{\partial x}\left(\frac{B}{H^2}\frac{\partial \psi}{\partial x}\right)+\frac{\partial}{\partial y}\left(\frac{B}{H^2}\frac{\partial \psi}{\partial y}\right)\right].\end{aligned} \tag{11}$$

Equation (11) can also be expressed as

$$\begin{aligned}V^{(n)} &= \frac{H}{\alpha}curl_z\left[\frac{\vec{\tau}_s-\rho_0\nabla\Omega}{\rho_0 H}\right]\\ &\quad-\frac{H}{\alpha}\left[\frac{\partial}{\partial x}\left(\frac{B}{H^2}\frac{\partial \psi}{\partial x}\right)+\frac{\partial}{\partial y}\left(\frac{B}{H^2}\frac{\partial \psi}{\partial y}\right)\right],\end{aligned} \tag{12}$$

where

$$\Omega = \frac{g}{\rho_0}\int_{-H}^0 z\rho dz, \quad \alpha = H\frac{\partial}{\partial n}\left(\frac{f}{H}\right). \tag{13}$$

$V^{(n)} = \vec{V}\cdot\vec{n}$, $\vec{n}$ is the unit vector normal to fH^{-1} contours. On the right-hand side of Eqs. (11) and (12), the first term is the main term. In particular, with $B = 0$, Eqs. (11)–(13) are reduced to equations (17)–(19) in Mertz and Wright (1992). As Mertz and Wright (1992) pointed out, Eqs. (11) and (12) emphasize JEBAR as a transport-generating term in that it enters (12) as a baroclinic forcing of flow across contours of fH^{-1}. Likewise for the IBWSR term. On the right-hand side of Eqs. (11) and (12), the second term is a resistance forcing of flow across contours of fH^{-1} due to the bottom friction. It is seen from the estimation of orders of magnitudes for Eq. (12) that the first term on the right-hand side of Eq. (12) is the main term. However, the second-order derivative terms in the second term on the right-hand side of Eq. (12) are not the main terms, and their order of magnitude is less. In the specific case $B = 0$, Eq. (12) expresses an explicit solution for transport, given a specified wind and density field.

The governing Eq. (9) for the stream function ψ satisfies the boundary conditions in the following two cases:

(1) On the open boundary condition:

In this computation, the values at the open boundaries are given by a modified inverse method (MIM) (Yuan *et al*., 1992). The values needed by the model include the barotropic and baroclinic transports across the open boundaries (see Fig. 1(b)).

(2) On the solid boundary condition: the stream function ψ = constant. The heavy lines in Fig. 1(a) denote the solid boundary condition.

If the values of ψ are known, with a constant vertical kinematic eddy viscosity coefficient A_z, the horizontal velocity components $\vec{v}(u, v)$ can be obtained by the

analytical expression with the aid of the stream function (see Yuan *et al*., 1986, 2007). The horizontal velocity components can be divided into four parts (Yuan *et al*., 1986, 2007) as follows:

$$u = u_\tau + u_G + u_B + u_I, \tag{14}$$

$$v = v_\tau + v_G + v_B + v_I, \tag{15}$$

where (u_τ, υ_τ) are the surface Ekman velocity components subject to the wind stress $\vec{\tau}$, (u_G, υ_G) are the geostrophic velocity components, (u_B, υ_B) are the bottom Ekman velocity components, which are almost zero outside the bottom Ekman layer, and (u_I, υ_I) are the velocity components due to baroclinic viscous effects. By definition, (u_I, υ_I) is zero at the sea floor, and the values are general less, as can be seen from comparison of the magnitude of the geostrophic velocity components term (u_G, υ_G). The explicit forms of the components in Eqs. (14) and (15) refer to Yuan *et al*. (1986, 2007).

Substituting formulas (14) and (15) for $\vec{v}(u, v)$ in the continuity equation and after vertically integrating the continuity equation with the boundary condition (3), we obtain the following approximate expression for the vertical component of velocity w outside the boundary layers (see Sarkisyan, 1977; Yuan *et al*., 2007):

$$w = \frac{1}{\rho_0 f} rot\vec{\tau}_s \cdot \vec{k} + \frac{\beta}{\rho_0 f^2}\tau_s^x + \frac{\beta z}{fH}\frac{\partial \psi}{\partial x} - \frac{zg\beta}{\rho_0 H f^2} \cdot \int_{-H}^{0}(H+z)\frac{\partial \rho}{\partial x}dz - \frac{g\beta}{\rho_0 f^2}\int_0^{-z}(-z+\varsigma)\frac{\partial \rho}{\partial x}d\varsigma. \tag{16}$$

The first term on the right-hand side of formula (16) is the vertical velocity component due to the action of curl wind stress, namely, the effect of Ekman pumping and the second term is the joint action between β effect and the wind stress $\vec{\tau}_s$. It is worth noting that the other terms on the right-hand side of formula (16) depend on z, while the first and second terms are independent of z. In particular, when $\beta = 0$, the vertical component of velocity w is reduced to w_1 only due to the effect of Ekman pumping

$$w_1 = \frac{1}{\rho_0 f} rot\vec{\tau}_s \cdot \vec{k}. \tag{16}'$$

3. Wind Data and Hydrographic Analysis

3.1 Wind data

The wind velocity field data with spatial resolution $2° \times 2°$ are extracted from ERS-1 and ERS-2. The kriging method with linear variogram model is adopted to interpolate all data into the calculated grid of $0.25° \times 0.25°$.

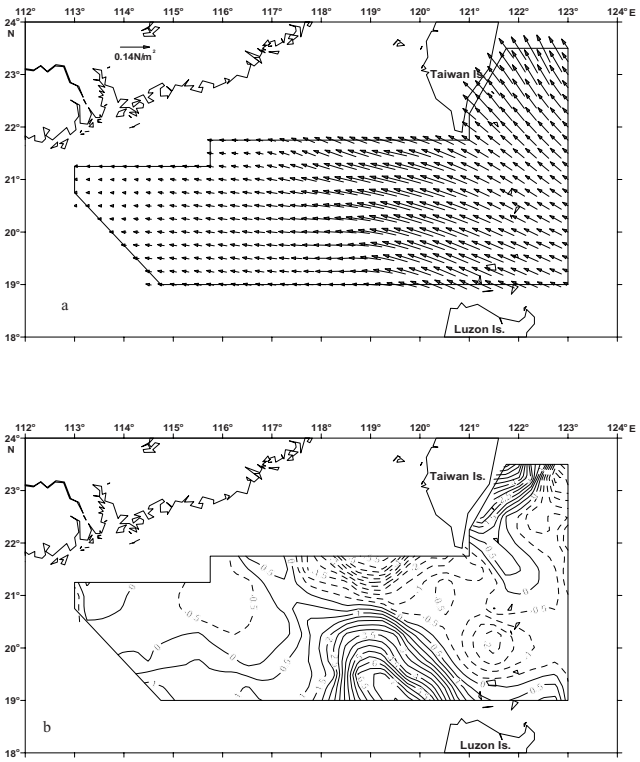

Fig. 2. (a) Wind stress (N/m^2) distribution; (b) curl wind stress distribution (10^{-7} N/m^3) in the computation region during August 28 to September 10, 1994.

Figures 2(a) and (b) show the distributions of the wind stress and the curl wind stress, respectively. From Fig. 2(a), the region east of 120°E is dominated mainly by the southeasterly wind, while the region west of 120°E is dominated mainly by the easterly wind. Figure 2(b) shows that the positive values of curl wind stress occur mainly in the regions northwest of Luzon Island and southeast of Taiwan Island. The maximum value of curl wind stress is about 8.0×10^{-7} N/m^3 in the area northwest of Luzon Island. The negative value of curl wind stress occurs mainly in the other part of the computed region.

3.2 Hydrographic analysis

The hydrographic data were obtained in the investigated regions southeast of Taiwan and near the Luzon Strait and in the northern South China Sea (SCS) during August 28 to September 10, 1994 during the cooperative cruises of the R/V Xiangyanghong No. 14, R/V Yanping No. 1, R/V Haiyan No. 1 and R/V Haiyan No. 3. We use also the kriging method with linear variogram model to interpolate all CTD data at observed stations into the calculated grid of $0.25° \times 0.25°$, and to obtain the horizontal distribution of water temperature, salinity and density. The

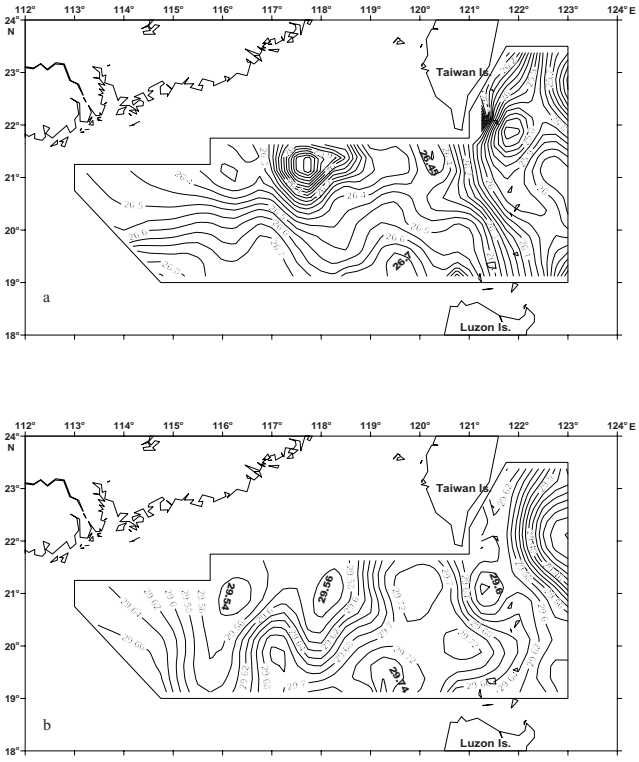

Fig. 3. Horizontal distribution of density (in σ_t) at (a) 200 m levels; (b) 600 m levels in the computation region during August 28 to September 10, 1994.

water depths at many hydrographic stations exceed 1200 m levels, but the maximum observed depth is only about 1200 m in these cruises. If the water depth at the hydrographic station is greater than 1200 m, the horizontal gradient of density ($\Delta\rho$) in this model is extrapolated according to the following formula (Sarkisyan, 1977):

$$\frac{\Delta\rho}{\Delta\rho_{1200}} = \frac{H - z}{H - 1200}.$$

Due to the limitation of space, figures of the horizontal distribution of water temperature and salinity are both omitted, and only the horizontal distribution of density at 200 and 600 m levels is shown here (Fig. 3). This is discussed further below.

1) The Kuroshio is located at the eastern part of the computed region and has higher temperature and lower density (Fig. 3). It has sub-high salinity surface water, high salinity in sub-surface water and a lower salinity middle layer water (Xu and Su, 1997). There is warm water with lower density in the area east of the main Kuroshio, centered near 22°10′ N.

2) As a rough estimate we consider that the boundary between the eastern part (the Northwest Pacific Water, NWPW) and western part (the South China Sea Water, SCSW) of Luzon Strait lies at about 121°E (Xu and Su, 1997).

Xu and Su (1997) pointed out from hydrographic analysis that a stronger northward current flows along the west coast of Luzon and round the northwest corner of Luzon Island, finally turning to the northeast. In the Bashi Channel, it mixes with the Kuroshio water, and is characterized by high temperature and lower salinity in winter and relatively low temperature and lower salinity in summer.

3) There is warm water with lower density in the area from 117°30′ E to 118°30′ E and 20°30′ N to 21°40′ N, centered at (21°00′ N, 118°00′ E) at the 20 m level, (21°00′ N, 117°45′ E) at the 200 m level, and (21°00′ N, 118°05′ E) at the 600 m level, respectively. The following computational results show that the circulation in the region with the warm water with lower density is the anticyclonic eddy W1 (Fig. 3).

4) There is cold water with higher density in the areas southwest of Taiwan Island and north of Luzon Island. The circulations in the regions with the cold water with higher density southwest of Taiwan Island and north of Luzon Island are, respectively, the cyclonic eddies CI and C2 (Fig. 3).

4. Diagnostic Current Results from Field Data by a Three-Dimensional Model with the Modified Inverse Method

Based on the hydrographic and wind data obtained in the investigated regions southeast of Taiwan and near the Luzon Strait and in the northern South China Sea (SCS) during August 28 to September 10, 1994, the circulation in the investigated area is computed using the three-dimensional diagnostic model of ocean circulation with a modified inverse method. The main computed results are described below.

4.1 Sectional distributions of the velocity at sections by the modified inverse method (MIM)

Figure 1(b) shows the location of observed hydrographic stations and the computation boxes in the computation region during August 28–September 10, 1994. The heavy lines in Fig. 1(b) denote the solid boundary condition. There are seven boxes (Fig. 1(b)). The computation points are at the mid-points between neighboring hydrographic stations. Each box is divided vertically into five layers with isopyncal $\sigma_{t,p}$ values of 25.0, 27.0, 30.0 and 35.0 at the four interfaces. For the vertical kinematic eddy coefficient A_z, Yuan *et al*. (1986, 1992) performed numerical experiments with different values of 10, 50, 100 m^2s^{-1}, and finally A_z was taken as 100 m^2s^{-1} according to the comparisons between computed results of cur-

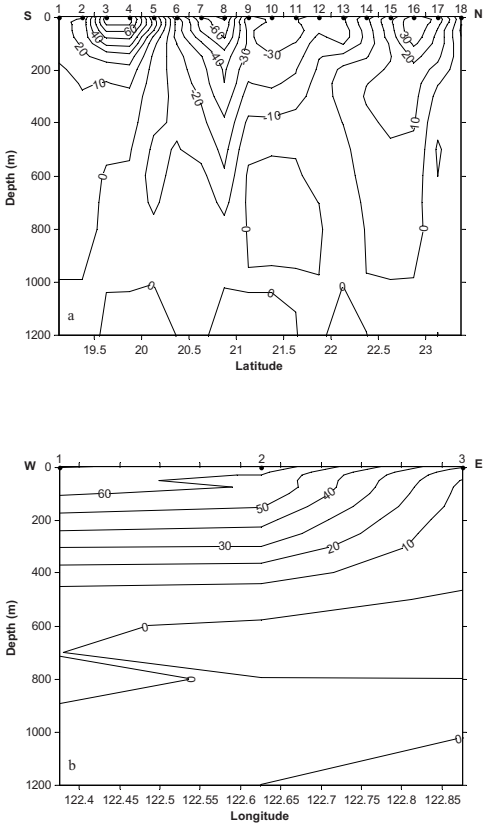

Fig. 4. Velocity distribution at Sections (a) HI (positive: eastward) (b) JI (positive: northward).

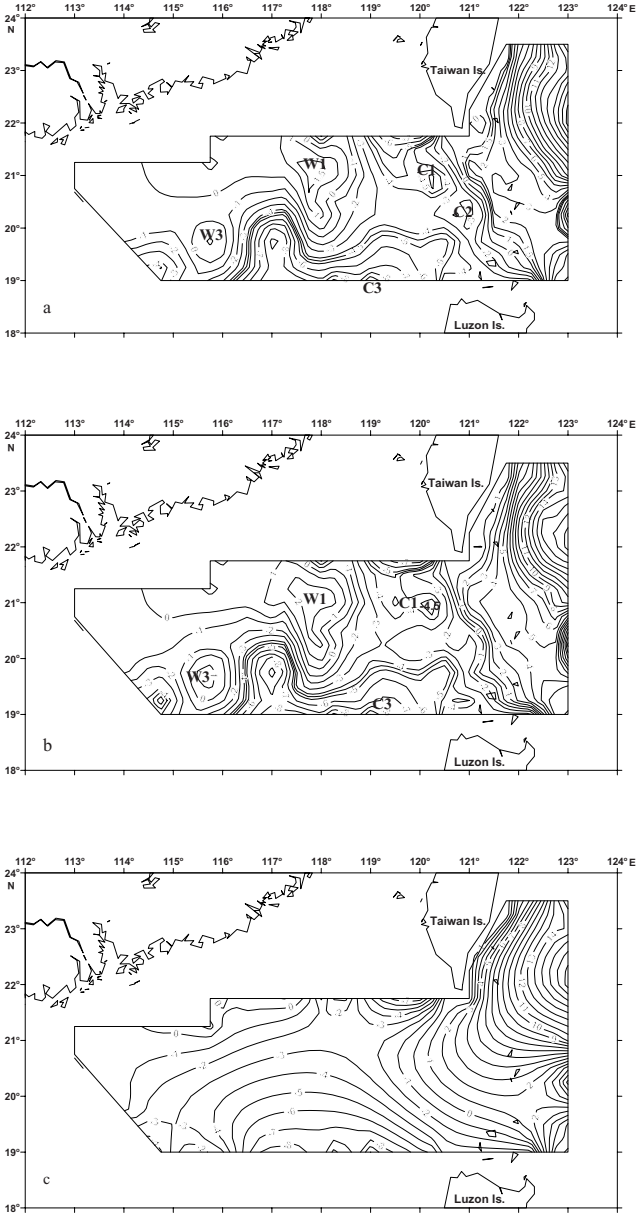

Fig. 5. Distribution of stream function and volume transport ($\times 10^6$ m^{3}s^{-1}) in the investigated region during August 28 to September 10, 1994 for (a) Case 2, (b) Case 3 and (c) Case 8.

rent for different values of A_z with the observed currents. However, they also found that the horizontal component of velocity vector $\vec{v} = (u, v)$ is not very sensitive to different values of A_z. The vertical eddy diffusivity K_v was taken as 10 m^{2}s^{-1} (Yuan *et al*., 1992).

Since space is limited, here we mainly discuss the sectional velocity distributions at Sections HI in the N-S direction, and JI and GH in the W-E direction (Fig. 1(b)), i.e., three sections in total. It is worth noting that the component of horizontal velocity perpendicular to the computed section can only be obtained in the MIM.

The main features of these sections of the investigated region found by the modified inverse method are as follows.

4.1.1 Section HI

Section HI lies in the N-S direction at 123°E (Fig. 1(b)). The Kuroshio flows westward through the section from the computation points 6 to 14, and its maximum velocity V_{max} is greater than 60 cm/s with a westward direction at the surface of computation point 8 (Fig. 4(a)). A part of the Kuroshio flows anti-cyclonically, turning to the northeast (see following Fig. 7), and then to the east through the north of Section HI from the computation points 14 to 18, and its maximum velocity V_{max} is greater than 30 cm/s with an eastward direction at the surface of computation point 16. At computation points 1 to 5, an eastward current occurs and its V_{max} is greater than 70 cm/s; it comes from the Kuroshio at Section JI (Figs. 4(a), (b) and following Fig. 7).

4.1.2 Section JI

Section JI is a latitudinal section at about 19°N (Fig. 1(b)). A branch of the Kuroshio, which comes from the

Table 1. Sensitivity experiments on the bottom friction coefficient, B, and topography effect.

Experiments	Name	B (ms^{-1})	Topography (H)	JEBAR	IBWSR	Figure
Experiments on B						
	Case 1	5×10^{-2}	√	√	√	omitted
	Case 2	1×10^{-2}	√	√	√	Fig. 7(a)
	Case 3	2.6×10^{-3}	√	√	√	Fig. 7(b)
	Case 4	1×10^{-3}	√	√	√	omitted
	Case 5	5×10^{-4}	√	√	√	omitted
	Case 6	0	√	√	√	omitted
Experiments on topography effect						
	Case 7	1×10^{-2}	× (H = 2000 m)	×	×	omitted
	Case 8	2.6×10^{-3}	× (H = 2000 m)	×	×	Fig. 7(c)

"√" means that the corresponding terms are considered, while "×" denotes that the corresponding terms are not considered.

west coast of Luzon, flows northward through Section JI from the computation points 1 to 3, and its maximum velocity V_{max} is greater than 60 cm/s with a northward direction at the surface of computation points 1 and 2 (Fig. 4(b)). This branch of the Kuroshio is located in the layer above about 500 m.

4.1.3 Section GH

Section GH is a latitudinal section at about 23.5°N (Fig. 1(b)). The Kuroshio flows northward through Section GH, and its maximum velocity V_{max} is about 90 cm/s with a northward direction near the Taiwan coast at the surface. The Kuroshio is located in the layer above about 1000 m.

4.2 Model configuration and sensitivity experiments

The diagnostic model domain is shown in Fig. 1(a). The horizontal grid sizes are taken as Δy = 27.8 km, $\Delta x = \Delta y \times \cos\theta$ = 27.8 km × $\cos\theta$, where θ is the latitude. When θ = 19.9°, f = 4.964 × 10^{-5} s^{-1} and β = 2.142 × 10^{-11} $s^{-1}m^{-1}$. The vertical grid levels are the standard levels. The value of the vertical kinematic eddy coefficient A_z, as above, was taken as 100 m^2s^{-1}. In addition, the bottom friction coefficient, B, is assigned in turn as 5×10^{-2}, 1×10^{-2}, 2.6×10^{-3}, 1×10^{-3} , 5×10^{-4} and 0 m s^{-1} (see Table 1). The dependence of the stream function ψ on these values of B and the topography effect is discussed below in terms of different cases of the sensitivity experiment (see Table 1).

For Case 3 ($B = 2.6\times10^{-3}$ ms^{-1}, Fig. 5(b)), the observed density and wind field are both considered, and the actual topography and β effect are also both considered (see Table 1). From Fig. 5(b), the main Kuroshio flows through Section HI from 20°30′ N to 22°10′ N, and then it moves anticyclonically. Most of the Kuroshio flows northward through Section GH into the region east of Taiwan Island, and a part of the Kuroshio flows eastward through the north of Section HI, as stated in Subsection 4.1. Next, a branch of the Kuroshio, which comes from the area near Luzon's eastern coast, flows northward through Section JI, as stated in Subsection 4.1, and it intrudes northwestward. It then branches again into western and eastern parts near 20°30′ N. Its eastern part flows northward into the area southeast of Taiwan, and its western part continues to intrude northwestward and flows through the area southwest of Taiwan.

The anti-cyclonic eddy W1 exists east of Dongsha Islands and in the area from 117°20′ E to 119°E and from 20°30′ N to 21°30′ N (Fig. 5(b)). The distribution of ADCP current vectors (Fig. 6) also revealed that this anti-cyclonic eddy W1 exists east of Dongsha Islands. Next, there is the cyclonic eddy C1 in the areas west of a northwestward intruded flow of the Kuroshio branch. These are the cyclonic eddy C3 in the area from 119°E to 120°E and the anti-cyclonic eddy W3 in the area from 115°10′ E to 116°10′ E near the southern boundary of the computational region (Fig. 5(b)).

Comparison of the hydrographic structure (Fig. 3) with the distribution of stream functions ψ in Case 3 (Fig. 5(b)) shows they agree qualitatively.

For Case 1 ($B = 5\times10^{-2}$ ms^{-1}), comparing Case 1 with Case 3 (Fig. 5(b)), they are some what different from each other. For example, the anti-cyclonic eddy W1 does

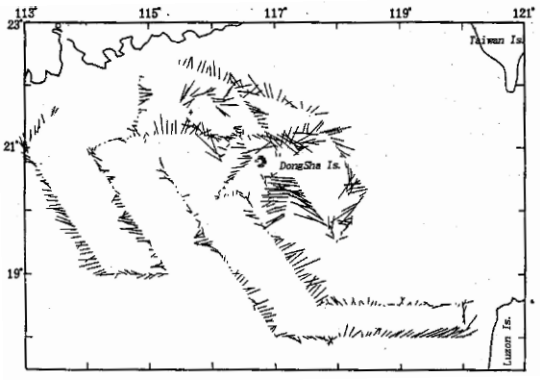

Fig. 6. Distribution of velocity (cm/s) from ADCP current observation at 40 m level during August 28 to September 10, 1994 (scale of speed is one degree latitude corresponds to a speed of 1.5 m s^{-1}, from Xu and Su, 1997).

Table 2. Percentage of the numbers of computed points for value of α lying at the variant interval (x, y), respectively, in the computed region and area east of 120°E (rate α = JEBAR/IBWSR).

The variant interval (x, y)	Computed region α	Area east of 120°E α
≤0.1	45.5%	39.2%
(0.1, 0.5]	0.8%	0%
(0.5, 1]	1.6%	0%
(1, 10)	7.2%	7.4%
>10	44.9%	53.4%

not seem to appear in the area east of Dongsha Islands in Case 1. This is because the bottom friction coefficient B is taken to be greater in Case 1.

For Case 2 (Fig. 5(a)) and Case 4, comparing Case 3 (Fig. 5(b)) with Case 2 (Fig. 5(a)) and Case 4, they agree basically and qualitatively, with only some quantitative changes.

When the value of B decreases from 5×10^{-4} (Case 5) to 0 ms^{-1} (Case 6), comparing Cases 5 and 6 with Case 3 (Fig. 5(b)), they show relatively great differences from each other, because the value adopted for bottom friction coefficient B is too small in Cases 5 and 6.

From the following model results of horizontal velocity, comparing the values of horizontal velocity for Case 2 ($B = 1 \times 10^{-2}$ ms^{-1}) with that for Case 3 ($B = 2.6 \times 10^{-3}$ ms^{-1}), the difference in their maximum velocity is slight, i.e. the differences of horizontal velocities between Case 2 and Case 3 are slight (see below, Subsection 4.4). From the above discussion, we take values of B in the range from 1×10^{-2} to 1×10^{-3} ms^{-1} to be reasonable values. In the following computation we discuss mainly Case 3 ($B = 2.6 \times 10^{-3}$ ms^{-1}).

4.3 Topography effect from stream function analysis

In order to examine the topography effect, Cases 7 and 8 (see Table 1) are examined with the same boundary conditions as Cases 1–6. However, the topography effect has not been considered, thus the main term, JEBAR, and the IBWSR term on the right-hand side of Eq. (12) both vanish in Cases 7 and 8 (Fig. 5(c)) (see Table 1). Comparing Cases 7 and 8 (Fig. 5(c)) with Case 2 (Fig. 5(a)) and Case 3 (Fig. 5(b)), we see they are very different from each other, and the patterns of circulation for Cases 7 and 8 (Fig. 5(c)) are relatively simple. In particula, the anticyclonic eddy W1 does not appear in the area east of Dongsha Islands, and none of the anti-cyclonic eddy W3 and cyclonic eddies C1 and C3 and so on occur, and the circulation in western part of the investigated region is dominated by the basin-scale cyclonic gyre (Fig. 5(c)). This phenomenon is not in agreement with observations (see Fig. 3), because there is no real forcing of flow across contours of fH^{-1} in Cases 7 and 8 (Fig. 5(c)).

To summarize, Eqs. (11) and (12) emphasize JEBAR as a transport-generating term in that it enters (12) as a baroclinic forcing of flow across contours of fH^{-1} (Mertz and Wright, 1992). Likewise, for the IBWSR term. When the term JEBAR and the IBWSR term on the right-hand side of Eq. (12) both equal zero, the real forcings, i.e., the barclinic forcing and the wind forcing, of flow across contours of fH^{-1} both vanish, which results in the patterns of circulation in Fig. 5(c) (Case 8). This shows that the joint effect of the baroclinity and relief (JEBAR) and the IBWSR terms are both important in different area (see Table 2) respectively for the real forcing of flow across contours of fH^{-1} in effecting the pattern of circulation.

4.4 Model results of horizontal velocity

4.4.1 Circulation system above 400 m levels

As above, the main Kuroshio flows through Section HI from 20°30′ N to 22°10′ N, and then it moves anticyclonically. Most of the Kuroshio turns to flow northward through Section GH into the region east of Taiwan Island, and part of the Kuroshio turns to flow eastward through the north of Section HI (Figs. 7(a) and (b)), as stated in Subsection 4.1.

A branch of the Kuroshio, which comes from the area near Luzon's eastern coast, flows northward through Section JI, as stated in Subsection 4.1, and intrudes northwestward. Next, there is a northward current, which comes from the area west of Luzon's western coast, and it turns to the northeast (or the east) in the area north of Luzon Island and south of the cyclonic eddy C2, when it then joins this intruded northwestward flow (Figs. 7(a) and (b)), which is coincident with the hydrographic analysis by Xu and Su (1997). This joint northwestward flow

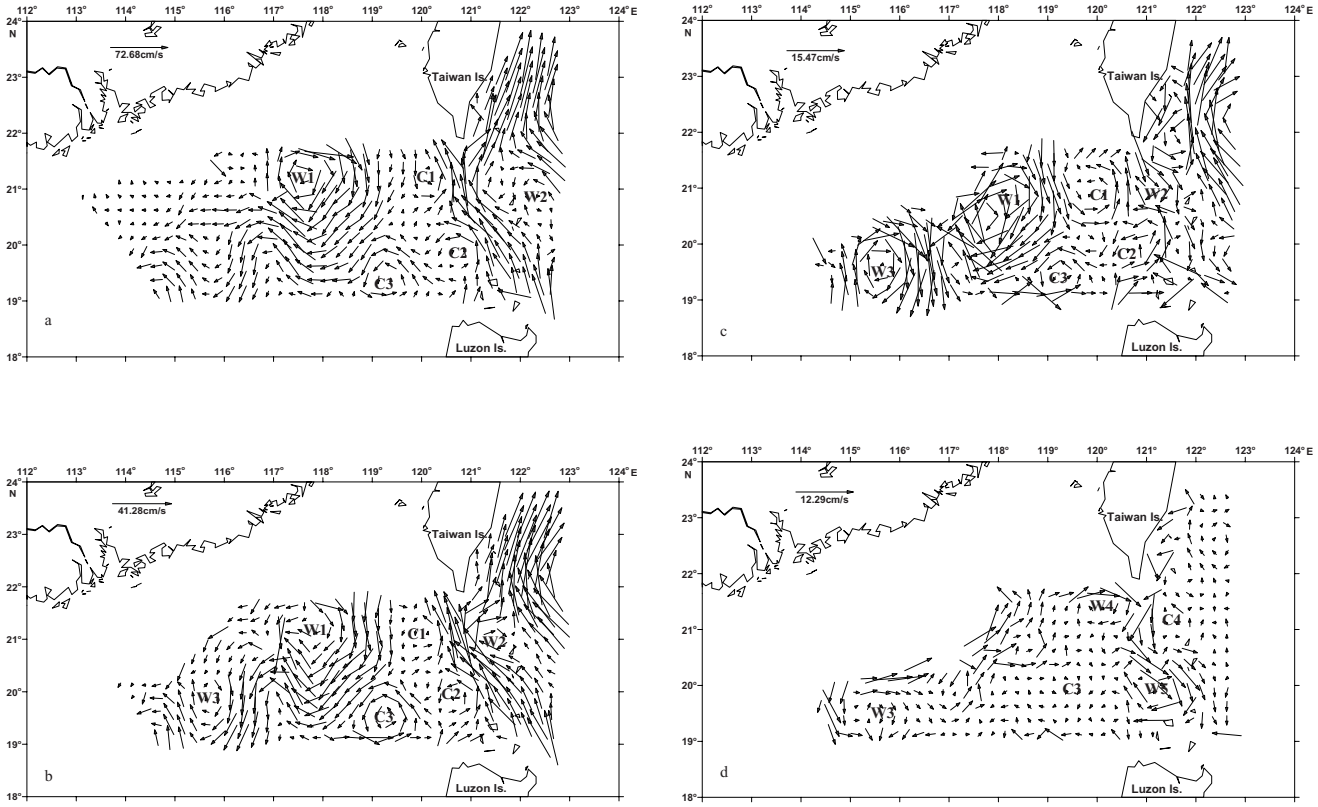

Fig. 7. Horizontal distribution of velocity vectors (cm/s) with $B = 0.0026$ ms^{-1} at (a) 100 m level; (b) 200 m level; (c) 500 m level; (d) 800 m level in the investigated region during August 28 to September 10, 1994.

branches the western and eastern parts near 20°30′ N. Its eastern part flows northward into the area southeast of Taiwan, while its western part continues to intrude northwestward into the SCS and flows through the area southwest of Taiwan (Figs. 7(a) and (b)).

On two sides of an intruded northwestward flow into the SCS there are cyclonic eddies C1 and C2 on its western side and the anti-cyclonic eddy W2 on its eastern side (Figs. 7(a) and (b)).

As shown in Figs. 7(a) and (b), the anti-cyclonic eddy W1 exists east of Dongsha Islands in the area from 117°30′ E to 118°30′ E and 20°30′ N to 21°40′ N. The distribution of ADCP current vectors also reveals that the anti-cyclonic eddy W1 exists east of Dongsha Islands (Fig. 6). Xu and Su (1997) and Yuan, D. L. *et al*. (2007) both pointed out that the anti-cyclonic eddy W1 originated northwest of Luzon. Next, in the computation region between 117°E and 121°E, except for the area of anti-cyclonic eddy W1, the circulation is mainly dominated by the basin-scale cyclonic gyre, and consists of the cyclonic eddies C1, C2 and C3. In the eastern part of the computation region below 200 m, we find the anti-cyclonic eddy W3.

4.4.2 Circulation system below 400 m

Above 1000 m, the Kuroshio flows through Section HI from 20°30′ N to 22°10′ N, and then moves anti-cyclonically. Most of Kuroshio turns to flow northward through Section GH into the region east of Taiwan Island, and part of the Kuroshio turns to flow eastward through the north of Section HI (Figs. 7(c) and (d)). However, there is a southward flow instead of the Kuroshio (northward current) in the northeastern part of the computation region at 1000 m depth.

In the region near the eastern coast of Taiwan below 400 m, we find the Taiwan costal southward current instead of northward current. It continues to flow southward, and then turns to flow southeastward (see Figs. 7(c) and (d)). Finally, it flows out through the southeastern boundary of the computation region (see Figs. 7(c) and (d)). This means that the Kuroshio is located near the eastern coast of Taiwan above 400 m and in the area east of the Taiwan costal southward current above 1000 m . In the area below 800 m, a southward current occurs instead of the Kuroshio (figure omitted).

Figures 7(c) and (d) reveal that: 1) the anti-cyclonic eddy W1 exists east of Dongsha Islands in a layer above

the 700 m level; 2) the cyclonic eddies C1 and C2 still exist in the layer above 700 m, and the anti-cyclonic eddies W4 and W5 occur in the layer below 700 m levels, instead of the cyclonic eddies C1 and C2; 3) the cyclonic eddy C3 exists in the layer above 1000 m levels; 4) the anti-cyclonic eddy W3 exists below 200 m levels.

We now compute the volume transport (VT) through sections CD and AB. Section CD is the latitude section from 118°30′ to 120°30′ E (see Fig. 1(b)). As above, a northward current flows from the area west of Luzon's western coast. The volume transport through the section CD is about 4.9×10^6 m^{3}s^{-1}. Section AB is the longitude section at 121°00′ E from 19°00′ N to 21°43′ N (see Fig. 1(b)). The net westward intruded volume transport through section AB is about 3.5×10^6 m^{3}s^{-1} in the layer above the 400 m level during August 28 to September 10, 1994. The net eastward VT through the section AB is about 0.22×10^6 m^{3}s^{-1} in the layer from the 400 m to 1200 m levels. The net westward VT through the section AB is about 0.22×10^6 m^{3}s^{-1} in the layer from the 1200 m to bottom. The above result seems to suggest that there is a sandwiched vertical structure in the mean LST (e.g., Qu, 2002; Yuan, 2002). Next, this value of net westward intruded VT seems to be larger than the climatological value in the layer above the 400 m level (see Qu, 2000; Qu *et al*., 2004), which may be because a weak El-Niño event occurred from August 1994 to March 1995. On an inter-annual time scale, the Luzon Strait transport tends to be higher during El-Niño years (Qu *et al*., 2004).

Finally, comparison of the horizontal velocity in Case 3 (Fig. 7, $B = 2.6 \times 10^{-3}$ ms^{-1}) with Case 2 ($B = 1 \times 10^{-2}$ ms^{-1}) shows they agree basically and qualitatively, with only some quantitative changes. For example, the difference in their maximum velocity is 2.06, 2.06, 0.44 and 1.69 cm/s, respectively, at 20 m, 200 m, 400 m and 1000 m levels, and the relative difference of their maximum velocity is about 2, 5, 2 and 13%, respectively, at 20 m, 200 m, 400 m and 1000 m levels. This shows that the horizontal velocity vector $\vec{v} = (u, v)$ is not very sensitive to different values of B, when we take the values of B in the range from 1×10^{-2} to 1×10^{-3} ms^{-1}.

4.5 Vertical component of velocity w

We now discuss the distribution of vertical component of velocity (VCV) w from August 28 to September 10, 1994, as follows.

At the surface layer, such as the 30 m level (see Fig. 8), the positive w value occurs in the following areas: it occurs mainly in the middle part of the computed region, namely, the most of the region of the basin-scale cyclonic gyre, and its maximum value of positive w is greater than 1.3×10^{-3} cm/s, located at the centre of cyclonic eddy C3, which is also the position of maximum value of the curl wind stress(see Fig. 2(b)). The negative w value occurs in the other region, where its maximum absolute value is less than 1×10^{-3} cm/s.

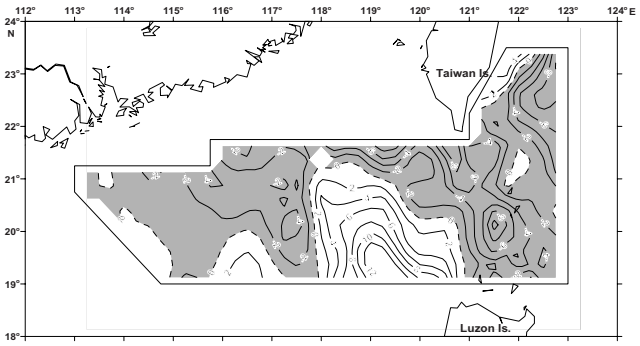

Fig. 8. Distribution of vertical component of velocity w (10^{-4} cm/s) at 30 m level with $B = 0.0026$ ms^{-1} in the investigated region during August 28 to September 10, 1994 (shaded parts: negative values; other parts: positive values).

Comparing the distribution of w at the 30 m level (see Fig. 8) with the distribution curl wind stress (see Fig. 2(b)), it is found that they agree basically in their change of signs, which shows that the dynamical cause of the vertical component of velocity w is mainly due to the effect of curl wind stress, i.e., the effect of Ekman pumping in the surface layer.

The following results have been obtained for the distribution of vertical component of velocity w in the subsurface layer, such as 200 m. Comparing the distribution of w at the 200 m level with Fig. 8, the range of positive value of w extends almost to the region occupied by the basin-scale cyclonic gyre, and its maximum value of positive w is less than 3.0×10^{-3} cm/s. The negative w value occurs in the other region, and its maximum absolute value is about 6×10^{-3} cm/s in the area south of Taiwan. In general, the absolute value of w in the subsurface layer is greater than that at the surface layer.

The following results for the distribution of vertical component of velocity w in the middle layer, such as 500 m and 800 m levels. Comparing the distribution of vertical velocity component w at 500 m and 800 m levels with that at the 200 m level, the changes in the range of positive and negative values of w are not large. The maximum value of positive w at 500 m and 800 m levels is about 5.0×10^{-3} cm/s and 6.0×10^{-3} cm/s, respectively. The negative w value occurs in the other region, and its maximum absolute value at 500 m and 800 m levels is about 9×10^{-3} cm/s and 1×10^{-2} cm/s, respectively, in the area south of Taiwan. In general, the absolute value of w in the middle layer is greater than that at the surface and sub-surface layers. Considering the dynamical cause of the distribution of vertical component of velocity w in the middle layer, one finds that the joint action between

the baroclinity and β effect and the joint action between the barotropy and β effect are both important, in addition to the effect of Ekman pumping.

The above discussion shows that the stronger upwelling occurs in the region occupied by the basin-scale cyclonic gyre, while the stronger downwelling occurs in the area south of Taiwan.

5. Conclusion

On the basis of hydrographic data obtained in the investigated regions near the Luzon Strait and in the northern SCS during August 28 to September 10, 1994, combined with the analysis of hydrographic and wind data, a three-dimensional diagnostic model of ocean circulation as well as a modified inverse method (MIM) were used to study the circulation in the investigated region. The main circulation features can be summarized as follows:

(1) The main Kuroshio

Near the eastern Taiwan coast, the Kuroshio is located above 400 m. However, the Taiwan costal southward current occurs below 400 m levels instead of a northward current. In the area east of the Taiwan costal southward current, the main Kuroshio is located above 800 m levels. In the area below 800 m levels, a southward current occurs instead of the main Kuroshio.

(2) A northwestward branch of the Kuroshio intrudes into the SCS through the Luzon Strait above 400 m levels.

A branch of the Kuroshio, which comes from the area near Luzon's eastern coast, joins with a part of the northward current, which comes from the area west of Luzon's western coast. This combined flow intrudes northwestward, and it branches into western and eastern parts near 20°30′ N. The eastern part flows northward into the area southeast Taiwan, while its western part continues to intrude northwestward into the SCS and flows through the area southwest of Taiwan.

(3) The net westward intruded volume transport through the longitudinal section AB at 121°00′ E from 19°00′ N to 21°43′ N is about 3.5×10^6 m^3s^{-1} in the layer above the 400 m level. The net eastward and net westward volume transports through the section AB are about 0.22×10^6 m^3s^{-1} and 0.22×10^6 m^3s^{-1}, respectively, in the layer from 400 m to 1200 m levels and the layer from the 1200 m to bottom. This seems to suggest that there is a sandwiched vertical structure in the mean LST (e.g., Qu, 2002; Yuan, 2002).

(4) The anti-cyclonic and cyclonic eddies

1) The anti-cyclonic eddy W1 exists in the area from 117°30′ E to 118°30′ E and 20°30′ N to 21°40′ N east of Dongsha Islands in a layer above the 700 m level; 2) On two sides of an intruded northwestward flow into the SCS, we find the cyclonic eddies C1 and C2 on its western side and the anti-cyclonic eddy W2 on its eastern side. The cyclonic eddies C1 and C2 exist in the layer above 700 m, while the anti-cyclonic eddies W4 and W5 occur in the layer below 700 m, instead of the cyclonic eddies C1 and C2; 3) The cyclonic eddy C3 exists in a layer above 1000 m; 4) The anti-cyclonic eddy W3 exists below 200 m levels in the eastern part of the computation region.

(5) The joint effect of the baroclinity and relief (JEBAR) and the IBWSR terms are both important in different area (see Table 2) respectively for the real forcing of flow across contours of fH^{-1} in effecting the pattern of circulation.

(6) Vertical component of velocity w

1) At the surface layer, the positive w value occurs mainly in the middle part of the computed region, namely, most of the region of the basin-scale cyclonic gyre. The dynamical cause of the vertical component of velocity w is mainly due to the effect of curl wind stress, i.e. due to the effect of Ekman pumping in the surface layer; 2) In the middle layer, comparing the distribution of w at 500 m and 800 m levels with that at 200 m levels, their changes of range of positive and negative values of w are not large. Considering the dynamical cause of the distribution of w in the middle layer, one finds that the joint action between the baroclinity and β effect and the joint action between the barotropy and β effect are both important, in addition to the effect of Ekman pumping.

Acknowledgements

This work was supported by the National Basic Research Program of China (No. 2007 CB816003), the International Cooperative Project of the Ministry of Science and Technology of China (No. 2006DFB21630) and the Key project of the National Natural Science Foundation of China (No. 40520140073) and Grant from the scientific research fund of the Second Institute of Oceanography, SOA (No. JG0715). We wish to thank the Oceanographic data center, State Key Laboratory of Satellite Ocean Environment Dynamics, Second Institute of Oceanography, SOA, for providing the CTD data.

References

Cai, S. Q., H. L. Liu, W. Li and X. M. Long (2005): Application of LICOM to the numerical study of the water exchange between the South China Sea and its adjacent oceans. *Acta Oceanol. Sinica*, **24**(4), 10–19.

Chu, P. and R. Li (2000): South China Sea isopycnal-surface circulation. *J. Phys. Oceanogr.*, **30**, 2419–2438.

Fang, G. H., Z. X. Wei, B. H. Choi, K. Wang, Y. Fang and W. Li (2002): Interbasin freshwater, heat and salt transport through the boundaries of the East and South China Seas from a variable-grid global ocean circulation model. *SCIENCE IN CHINA (Series D)*, **46**(2), 149–161.

Liu, Y. G., Y. C. Yuan, J. L. Su and J. Z. Jiang (2000): Circulation in the South China Sea in summer 1998. *Chinese Sci. Bull.*, **45**(18), 1648–1655.

Mertz, G. and D. G. Wright (1992): Interpretations of the JEBAR Term. *J. Phys. Oceanogr.*, **22**, 301–305.

Qu, T. D. (2000): Upper-layer circulation in the South China Sea. *J. Phys. Oceanogr.*, **30**, 1450–1460.

Qu, T. D. (2002): Evidence for water exchange between the South China Sea and the Pacific Ocean through the Luzon Strait. *Acta Oceanol. Sinica*, **21**(2), 175–185.

Qu, T. D., Y. Y. Kim, M. Yaremchuk, T. Tozuka, A. Ishida and T. Yamagata (2004): Can Luzon Strait transport play a role in conveying the impact of ENSO to the South China Sea? *J. Climate*, **17**, 3643–3656.

Sarkisyan, A. S. (1977): The diagnostic calculations of a large-scale oceanic circulation. p. 363–458. In *The Sea*, Vol. 6, ed. by E. D. Goldberg, I. N. McCave, J. J. O'Brien *et al.*, A Wiley-Interscience Publication, New York.

Xu, J. P. and J. L. Su (1997): Hydrographic analysis on the intrusion of Kuroshio into the South China Sea-II. Observational results during the cruise from August to September in 1994. *Tropic Oceanology*, **16**(2), 1–23 (in Chinese with English abstract).

Xu, J. P., J. L. Su and D. H. Qiu (1995): Hydrographic analysis on the intruding of Kuroshio water into the South China Sea. *Proceeding of the Symposium on the Oceanic Science in the Taiwan Strait and Its Neighboring Regions*, p. 30–43, China Ocean Press, Xiamen.

Xue, H., F. N. Pettigrew and D. Xu (2004): Kuroshio intrusion and the circulation in the South China Sea. *J. Geophys. Res.*, **109**, C02017, doi:10.1029/2002JC001724.

Yuan, D. L. (2002): A numerical study of the South China Sea deep circulation and its relation to the Luzon Strait transport. *Acta Oceanol. Sinica*, **21**(2), 187–202.

Yuan, D. L., W. Q. Han and D. X. Hu (2007): Anti-cyclonic eddies northwest of Luzon in summer–fall observed by satellite altimeters. *Geophys. Res. Lett.*, **34**, L13610, doi:10.1029/2007GL029401.

Yuan, Y. C. and J. L. Su (1988): The calculation of Kuroshio Current Structure in the East China Sea—Early summer 1986. *Prog. Oceanogr.*, **21**, 343–361.

Yuan, Y. C., J. L. Su and S. Y. Xia (1986): A diagnostic model of summer on the northwest of the East China Sea. *Prog. Oceanogr.*, **17**, 163–176.

Yuan, Y. C., J. L. Su and Z. Q. Pan (1992): Volume and heat transports of the Kuroshio in the East China Sea in 1989. *La mer*, **30**, 251–262.

Yuan, Y. C., R. Y. Lou, Y. G. Liu, J. L. Su, K. S. Wang and H. Chen (2005): Currents in the Luzon Strait during spring of 2002: Observation and Computation by modified inverse model. *Acta Oceanol. Sinica*, **24**(1), 1–13.

Yuan, Y. C., G. H. Liao and X. H. Xu (2007): Three dimensional diagnostic modeling study of the South China Sea circulation before onset of summer monsoon in 1998. *J. Oceanogr.*, **63**(1), 77–100.